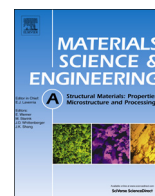




ELSEVIER

Contents lists available at ScienceDirect

Materials Science & Engineering A

journal homepage: www.elsevier.com/locate/mseaSulfide stress cracking resistance of the welded WDL690D HSLA steel in H₂S environmentF. Huang^{a,*}, S. Liu^a, J. Liu^a, K.G. Zhang^b, T.H. Xi^b^a College of Materials Science and Metallurgical Engineering, Wuhan University of Science and Technology, Wuhan, Hubei 430081, China^b Research and Development Center, Wuhan Iron and Steel (Group) Corporation, Wuhan 430080, China

ARTICLE INFO

Article history:

Received 4 August 2013

Received in revised form

22 October 2013

Accepted 25 October 2013

Available online 31 October 2013

Keywords:

WDL690 steel

Welded joint

Hydrogen embrittlement

Hydrogen permeation

ABSTRACT

Sulfide stress cracking resistance of welded high strength low alloy (HSLA) steel for high pressure vessel (called “WDL690D” steel) was evaluated in NACE “A” solution at room temperature. Though the failure time increased with the decreasing applied stress for either WDL690D base steel or its welded joint, the welded joint presented the lower threshold stress of about 53% YS compared with the base steel of about 65% YS, because of its inhomogeneous microstructure distribution. The hydrogen trapping efficiency of the WDL690D base steel and its welded joint was also investigated by measuring the permeability $J_{\infty}L$ and the apparent diffusivity (D_{app}). The results showed that the welded joint had lower trapping efficiency, but was more susceptible to SSC. In addition, the fractography of both the WDL690D base steel and its welded joint all exhibited a mixed ductile-brittle rupture when exposed in H₂S environment under constant loading stress.

© 2013 Elsevier B.V. All rights reserved.

1. Introduction

High strength low alloy (HSLA) steels used for high pressure vessel or pipeline in the storage and transportation of oil and gas that contain H₂S are limited due to the mechanical and corrosion problems induced by H₂S. Two of the major damage phenomena in H₂S environment are sulfide stress cracking (SSC) and hydrogen induced cracking (HIC) [1–4].

SSC is a hydrogen embrittlement phenomenon in which crack failures can occur in stresses well below the yield strength of the material [5]. When steels are exposed to a wet H₂S environment, hydrogen atoms are produced as a result of the cathodic reduction of the proton (H⁺) that accompanies the anodic oxidation of iron. The hydrogen atoms could combine to form molecular gaseous hydrogen. However, the recombination reaction of hydrogen atoms to form molecular hydrogen is retarded on the steel surface due to the presence of H₂S or hydrogen sulfide ion (HS⁻) [6–8]. As a result, some atomic hydrogen diffuses into the steel. According to the model proposal by Troiano [9] and Oriani [10], the local atomic cohesive force decreased in the presence of hydrogen, under constant load, the hydrogen concentration at grain boundaries on the surface of the sample has the maximum, which increase with time by stress-induced diffusion, when the hydrogen concentration at grain boundaries reaches a critical value, which is necessary for crack initiation, cracking occurs [11].

The presence of inclusions is an important factor affecting hydrogen embrittlement susceptibility [12]. The susceptibility to hydrogen embrittlement is closely related to the steel composition and the processing history because these parameters affect the formation of nonmetallic inclusions (type, size and morphology) and the material's ability to accommodate hydrogen. Large inclusions such as elongated manganese sulfides and stringers of oxide increase the HIC susceptibility [13]. Domizzi et al. [14] showed that the HIC susceptibility depended on the sulfur content, average length and total length per unit area of the sulfide inclusions. Our group found that different types of inclusions in the steel play different roles in crack initiation, the inclusions rich in Mn and Al acted as the initiation sites for HIC cracking, and no HIC cracks were observed at inclusions rich in Si [12,15].

SSC and HIC behavior depend not only on steel cleanliness but also on its microstructure [16,17]. Boniszewski and Watkinson clearly demonstrated that both hardness and microstructure influence the susceptibility of low alloy steels to hydrogen embrittlement through extensive work on the heat affected zones of welded steels [14]. Cracking initiates and propagates more easily in the less ductile microstructures. So, segregated zones with bainitic or martensitic structures are harmful [18]. Carneiro et al. [19] showed that the refined and homogeneously quenched and tempered bainite/martensite microstructure had the best performance against HIC and SSC. On the other hand, other researchers found that acicular ferrite and ultrafine ferrite have the optimum HIC resistance as well as the good mechanical properties; the resistance against SSC is better for acicular ferrite than for ultrafine ferrite [20]. Also, a non-quench ageing process was proposed to provide higher strength and better

* Corresponding author. Tel.: +86 27 68862632; fax: +86 27 68862529.
E-mail addresses: Huangfeng@wust.edu.cn, hgxl@163.com (F. Huang).

SSC resistance for acicular ferrite pipeline steels, without affecting their microstructures [21]. Park et al. found that acicular ferrite was the most efficient microstructure for hydrogen trapping, whereas the deformed pearlite was the least efficient [22].

The WDL690D HSLA steels are regarded as the most promising steel for high pressure vessel applications in 21 century due to its high-strength and good ductility. In practice using, the WDL690D steels are welded to form pressure vessel, and the microstructure at the weld joint zone may be adversely affected by the welding process, resulting in decrease in corrosion resistance, especially in wet H₂S environments. Du et al. [23] showed that in Ku'erle soil the corrosion rate of X70 steel with original microstructure was the lowest among the different microstructures obtained by water quenching, air cooling and furnace cooling. Microstructural hardening and grain coarsening increased stress corrosion cracking (SCC) susceptibility of the X70 steel in simulating solutions of acidic soil in Yingtan in south-east China, and it was also observed that hydrogen was actively involved in the SCC process [24]. Huang et al. [12,15] found that the lower the values of D_{app} and $J_{\infty}L$ and the larger the value of c_{app} , the more the hydrogen was entrapped in the steel and the larger the HIC susceptibility of the X80 and X120 steel. Nonetheless, the differences of SSC susceptibility and hydrogen diffusion between the base steel and its welded joint in HSLA high pressure vessel steels have not been examined in detail. Therefore, it is necessary to study the relationship between various microstructures and hydrogen diffusion in order to understand clearly the different SSC behaviors between the base steel and its welded joint of WDL690D steel induced by hydrogen.

In this work, the proof ring testing per NACE TM-0177 and the electrochemical polarization techniques were used to measure SSC threshold stress value and the corrosion rate of welded WDL690D steel in NACE A solution. The morphology and microstructure of weld metal, HAZ and based steel were characterized by optical microscopy and scanning electron microscopy (SEM). The fractography and the correlation between SSC susceptibility, microstructure and the hydrogen permeability under constant load of base steel and its welded joint were discussed in detail.

2. Experimental procedures

2.1. Tested material and welding procedure

The HSLA steel for high pressure vessel was supplied by Wuhan Iron and Steel Corporation (marked as “DWL690” steel), and welds were deposited using the submerged-arc welding (SAW) process. Table 1 summarizes the chemical composition of the “DWL690 steel” base metal and weld metal (J707RH). The chemical composition was analyzed by inductive coupled plasma (ICP).

2.2. Microstructure analysis

For microstructure analysis, the welding joint specimen of the WDL690D steel was wet-ground with silicon carbide papers up to 1200 grit, and then polishing in 6 and 1 μm diamond suspension. After that, the specimen was then etched with 4% nital (4 ml nitric acid + 98 ml ethyl alcohol). The surface was examined under field

emission-Scanning electron microscopy (FE-SEM) (Czechoslovakia Nova nano 400 with an energy dispersive X-ray spectrometer (EDX).

2.3. Electrochemical testing

All electrochemical tests were conducted at 25 °C and atmospheric pressure. Tests were made using a standard glass cell containing the working electrode (specimen) and a Pt counter electrode. Potentials were measured with reference to a saturated calomel electrode (SCE) interfaced to the test solution via a salt bridge that terminated about 2 mm from the specimen. Schematic diagram of the sealing three-electrode system was shown in Fig. 1. PARSTAT 2273 Advanced Electrochemical System was utilized to perform the potentiodynamic polarization.

NACE TM-0177 test solution “A” was used in all electrochemical tests. Test solution “A” consisted of an acidified H₂S saturated aqueous environment containing 5.0 wt% NaCl and 0.5 wt% CH₃COOH. After pouring the solution and sealing the cell, the cell was deaerated by nitrogen gas (99.9%) for 1 h to eliminate any oxygen interference with the electrochemical reaction. After purging, H₂S was bubbled into the cell at a flow rate of 50 cc/min for 30 min before starting the test.

After preparing and sealing the electrochemical cell, the test specimen was immersed in the test solution for 30 min in order to measure the open circuit potential (E_{OCP}). After reaching a stable open circuit potential (E_{OCP}), the electrode potential was swept potentiodynamically at a scan rate of 1.66 mV/s from an initial potential of –0.15 V to 0.5 V versus open circuit potential.

2.4. SSC constant load testing

Test procedure was conducted as per NACE TM-0177. All proof ring tests were conducted at room temperature. Fig. 2 shows a schematic arrangement for SCC test. The environmental test chamber was secured by O-ring seals that prevented any leakage during testing.

The amount of deflection needed to apply the desired load with the proof ring was determined by using the calibration curves of each

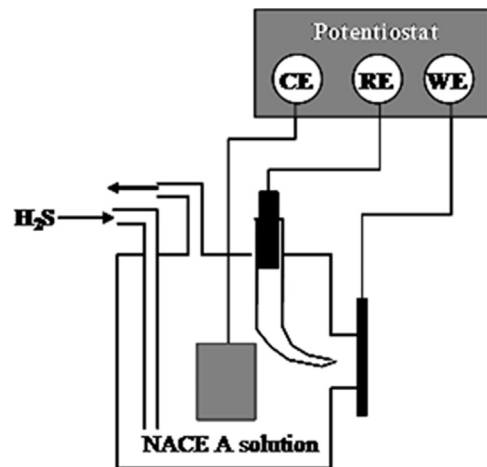


Fig. 1. Schematic diagram of the sealing three-electrodes system.

Table 1
Chemical composition of the DWL690 steel and weld metal.

Sample	C	Si	B	Mn	P	S	Al	Als	Ni	Cr	Ti	Mo	V	Nb
Base metal	0.0772	0.313	0.0007	1.483	0.008	0.0049	0.029	0.0273	0.464	0.019	0.012	0.183	0.04	0.03
Weld metal	0.0821	0.0432	/	1.323	0.015	0.016	/	/	1.581	0.092	/	0.394	/	/

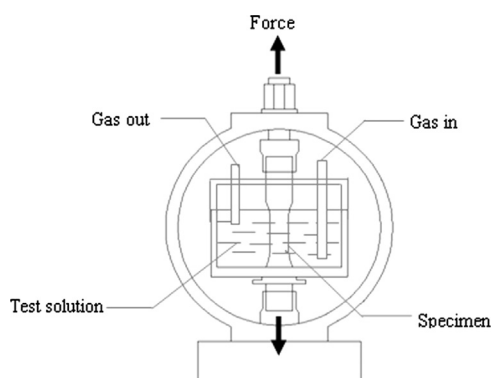


Fig. 2. Uniaxial tensile testing (constant load).

proof ring. Loads for stressing the specimens were determined from the following equation:

$$P = S \times A \quad (1)$$

where P =load, S =applied stress and A =actual cross section area of the gauge section. The specimens were loaded at stress values equivalent to different percentages of the material's Yield stress value (90%, 72%, 65%, 60%, 55%, 50%, 45%, 40%). The corresponding time - to-failure (TTF) was recorded. Determination of SCC susceptibility using this technique was based on the TTF for maximum test duration of 720 h (30 days). An automatic timer attached to the test specimen recorded the TTF. The cracking susceptibility was expressed in terms of a threshold stress (σ_{th}) for SCC below which cracking did not occur during the maximum test duration. In all tests initial and final pH values were measured for each test.

The fracture surfaces of the failed test specimens were cleaned in 500 mL HCl+500 mL H₂O+6.5 g hexamethylenetetramine to remove the corrosion product, and then dipped in acetone for 5 min. The fracture surfaces were observed by FE-SEM.

2.5. Hydrogen permeation test

The hydrogen diffusion behavior of WDL690D base steel and its welded joint was investigated by the hydrogen permeation test which was performed in a dual cell called "modified Devanathan-Stachurski cell" used in our previous research [12,15]. Two samples were prepared with the surface area of $20 \times 20 \text{ mm}^2$ and the thickness of 1.07 mm. Both sides of the specimens were polished to eliminate flux-limiting surface impedances and to ensure the reliability of the hydrogen oxidation current. The specimens were mounted between the two cells with a 1.00 cm^2 area exposed to each electrolyte cells. The deaerated 0.1 mol/L NaOH solution and the deaerated NACE TM-0177 "A" solution, same as that for SCC constant load testing and electrochemical testing were selected as test solutions in the hydrogen oxidation cell and the hydrogen charging cell, respectively. The potential of the steel membrane on the hydrogen oxidation cell was maintained at a potential of 250 mV_{SHE} , with the domination oxidation reaction to be oxidation of hydrogen that diffused through the steel membrane. During the hydrogen permeation test, the potential was not applied, and the H₂S gas was bubbled continuously through the NACE A solution to maintain a positive pressure.

The apparent hydrogen diffusivity in steels can be determined by the relaxation time obtained from the hydrogen permeation curve [15,22,26]. The relation between the steady-state current (I_{∞}), the thickness of specimen (L), the relaxation time (t_L), the permeability ($J_{\infty}L$), the apparent hydrogen diffusivity (D_{app}) and the apparent hydrogen solubility (c_{app}) are converted according to

the following Eqs. (2)–(4):

$$J_{\infty}L = \frac{I_{\infty}L}{FA} \quad (2)$$

$$D_{app} = \frac{L^2}{6t_L} \quad (3)$$

$$c_{app} = \frac{J_{\infty}L}{D_{app}} \quad (4)$$

where F is Faraday constant and A is area of sample exposed to each electrolyte cells, respectively.

In addition, the hydrogen trap density can be estimated according to the following equation [27]:

$$N_T = \frac{C_{app}}{3} \left(\frac{D_1}{D_{app}} - 1 \right) \quad (5)$$

where N_T is the number of hydrogen trapping sites per unit volume and D_1 the lattice diffusion coefficient. Substituting $D_1 = 1.28 \times 10^{-4} \text{ cm}^2 \text{ s}^{-1}$, which is the diffusivity of α -Fe [25].

All experiments were performed at room temperature. In order to ensure the reliability of the experimental data, each test was repeated at least three times. Some were conducted five times for confirmation.

3. Results

3.1. Microstructure, strength and hardness

Fig. 3 shows the optical view of macrostructure around the WDL690D welded joint. Weld metal, fusion line and HAZ were observed obviously. To further characterize the microstructure of the various zones around weld, FE-SEM views were shown in Fig. 4. It is seen that the microstructure of weld metal (Fig. 4d) consisted of acicular ferrite and grain boundary ferrite. Moreover, holes were observed in the weld metal zone, which were introduced during welding operation. While that of heat-affected zone is a mixture of acicular ferrite, bainitic ferrite and a few martensite/austenite microconstituents. The microstructure of base steel is typically ferrite and pearlite, with apparent austenite grain boundary network. The microstructure of steels had its effect on the material's strength value. The yield strengths for the WDL690D base steel and its welded tested steel were determined by pulling tensile specimens in air. The engineering yield strength for base steel and its welded steel were 743 MPa and 560 MPa, respectively.

The Vickers hardness distribution of the middle portion of the weld zone across the welded joint was shown in Fig. 5. It is seen

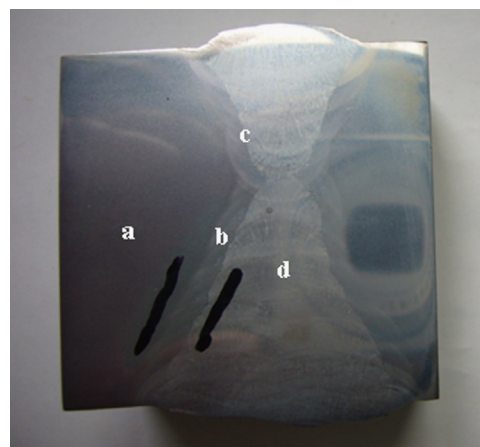


Fig. 3. Observation of welded HSS steel by optical camera (a) base steel; (b) HAZ; (c) HAZ/weld metal and (d) weld metal.

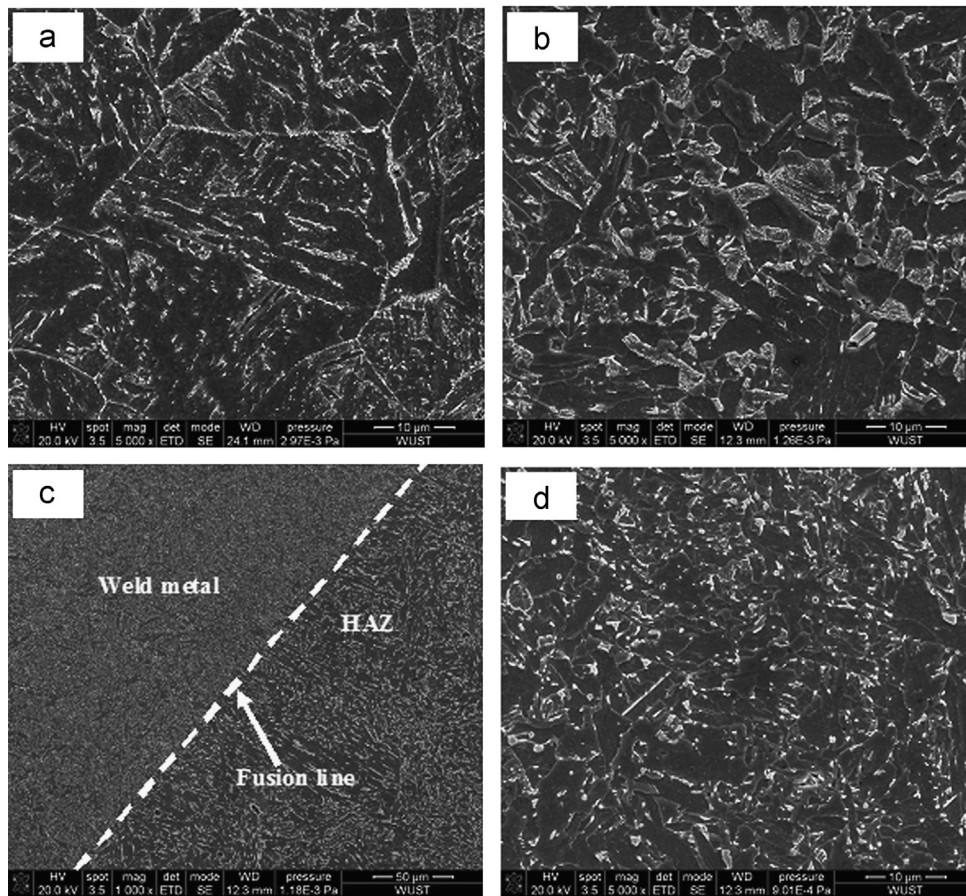


Fig. 4. SEM observation of welded high pressure vessel steel (a) base steel; (b) HAZ; (c) HAZ/weld metal and (d) weld metal.

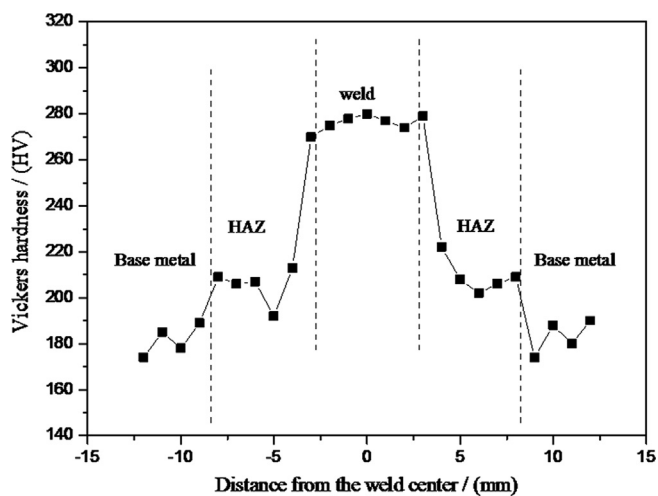


Fig. 5. Hardness distribution of the WDL690 base steel and its welded joint.

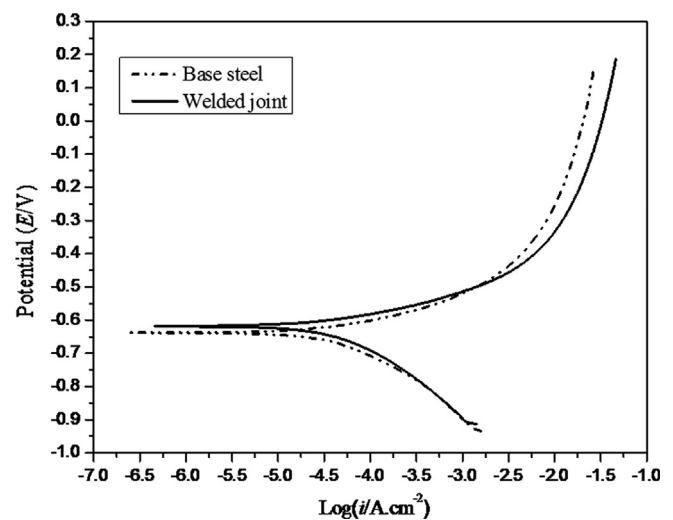


Fig. 6. The polarization curves of the WDL690 base steel and its welded joint.

that there was an approximately normal distribution of the measured hardness. The largest hardness occurred on weld metal of about 270–280 HV. The hardness value decreased from the weld metal to HAZ. There was the smallest hardness on the base steel of about 170–190 HV.

3.2. Electrochemical behavior

Before conducting the polarization test, open circuit potential measurement for WDL690D base steel and its welded joint in H_2S saturated NACE TM-0177 “A” solution was carried over 30 min. For

those two specimens, the potential readings were slightly fluctuating in the first 300 s, and then started to decrease until a steady state E_{OCP} of about -0.64 V and -0.61 V for WDL690D base steel and its welded joint respectively, and the E_{OCP} of the base steel is slightly more negative than that of the welded joint.

The polarization curves for the WDL690D base steel and its welded joint in H_2S saturated NACE TM-0177 “A” solution was shown in Fig. 6. The anodic curves showed linear Tafel behavior until about -0.5 V and -0.4 V. At those potential, FeS corrosion products formed on the surface of the WDL690D base steel and its

welded joint, the corroded surface became darker with applied potentials increasing. After -0.5 V and -0.4 V, the current density just continued to increase very slowly with potential increasing. Some of the produced corrosion product started to spall off the specimen. The corrosion current densities (i_{corr}) were found to

$63.9 \mu\text{A}/\text{cm}^2$ and $158 \mu\text{A}/\text{cm}^2$ for the base steel and its welded joint respectively by extrapolating the linear Tafel slopes. The initial pH was 2.73 and the pH at the end of the test was 2.98 and 3.42 for the base steel and its welded joint, respectively. The increase in bulk pH was due to the consumption of hydrogen ions to form hydrogen gas (atomic or molecular) as part of the cathode reaction: $2\text{H}^+ + 2\text{e}^- \rightarrow \text{H}_2$ or 2H . Apparently, the natural corrosion current density of the base steel is much lower than that of the welded joint.

Table 2

Proof ring test results tested in NACE TM-0177 "A"(25 °C). Dashed lines (–) in the time to failure column indicate that the specimen survived the 720 h (1 month) test duration.

% YS	Specimen	pH initial/final	Time to failure (h)	Result	Overall result
90	1	2.68/2.94	24	Fail	Fail
	2	2.68/2.88	10	Fail	
	3	2.68/2.94	26	Fail	
72	1	2.68/2.98	54	Fail	Fail
	2	2.68/3.12	66	Fail	
	3	2.68/2.98	58	Fail	
65	1	2.68/4.10	–	Pass	Pass
	2	2.68/3.92	–	Pass	
	3	2.68/3.85	–	Pass	
60	1	2.68/3.84	–	Pass	Pass
	2	2.68/3.98	–	Pass	
	3	2.68/4.08	–	Pass	
50	1	2.68/3.96	–	Pass	Pass
	2	2.68/4.12	–	Pass	
	3	2.68/3.84	–	Pass	
45	1	2.68/3.94	–	Pass	Pass
	2	2.68/3.87	–	Pass	
	3	2.68/3.96	–	Pass	
40	1	2.68/3.76	–	Pass	Pass
	2	2.68/3.78	–	Pass	
	3	2.68/3.96	–	Pass	

Table 3

Proof ring test results of the DWL690 steel welded joint in NACE TM-0177 "A": (25 °C). Dashed lines (–) in the time to failure column indicate that the specimen survived the 720 h (1 month) test duration.

% YS	Specimen	pH initial/final	Time to failure (h)	Result	Overall result
90	1	2.68/2.72	2	Fail	Fail
	2	2.68/2.78	3.5	Fail	
	3	2.68/2.84	8	Fail	
72	1	2.68/2.98	12	Fail	Fail
	2	2.68/3.12	10	Fail	
	3	2.68/2.98	8	Fail	
65	1	2.68/4.10	14	Fail	Fail
	2	2.68/3.92	12	Fail	
	3	2.68/3.85	18	Fail	
60	1	2.68/3.84	20	Fail	Fail
	2	2.68/3.98	28	Fail	
	3	2.68/4.08	32	Fail	
55	1	2.68/3.96	252	Fail	Fail
	2	2.68/3.89	248	Fail	
	3	2.68/3.98	296	Fail	
50	1	2.68/3.96	–	Pass	Pass
	2	2.68/4.12	–	Pass	
	3	2.68/3.84	–	Pass	
45	1	2.68/3.94	–	Pass	Pass
	2	2.68/3.87	–	Pass	
	3	2.68/3.96	–	Pass	
40	1	2.68/3.76	–	Pass	Pass
	2	2.68/3.78	–	Pass	
	3	2.68/3.96	–	Pass	

3.3. Proof ring testing

3.3.1. Threshold stress σ_{th} determination

As seen in Table 2, twenty-one base steel tensile specimens were grouped into seven sets that were stressed at different percentages of the yield strength (90%, 72%, 65%, 60%, 50%, 45%, 40%) in the NACE TM-0177 "A" solution (saturated H_2S) until breakage or a maximum test duration of 720 h (1 month).

Twenty-four welding joint tensile specimens were grouped into eight stressed at different percentages of the yield strength (90%, 72%, 65%, 60%, 55%, 50%, 45%, 40%), as shown in Table 3, also in the NACE TM-0177 "A" solution (saturated H_2S) until breakage or a maximum test duration of 720 h (1 month).

The results from Tables 2 and 3 were plotted in Figs. 7 and 8, respectively. It can be seen that the time to failure for both the

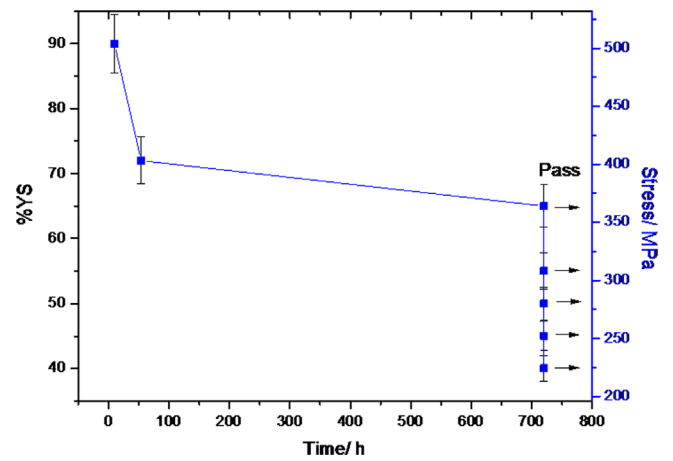


Fig. 7. Proof ring time to failure for the Dbase steel in the NACE TM-0177 A solution.

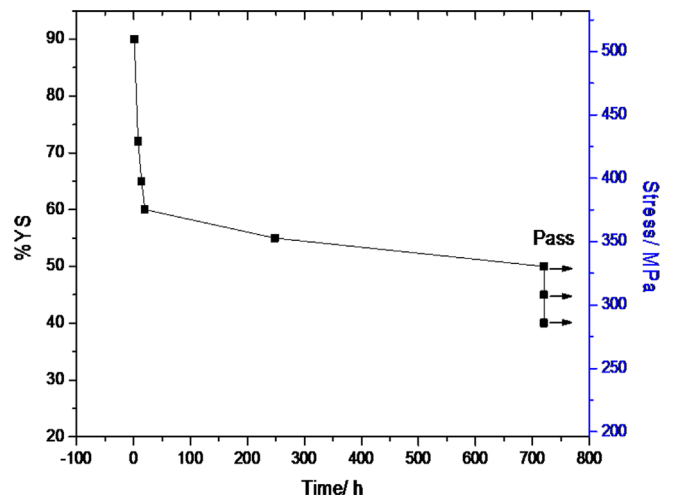


Fig. 8. Proof ring time to failure for the Dsteel welded joint in the NACE TM-0177 A solution.

based steel and the welded joint increased with a decrease in the applied load. In addition, the change of time to failure values between two consecutive applied stresses seemed to widen as the threshold stress value was approached. For the DWL690 base steel, an applied stress of 72% YS generated a “fail” result while 65% YS generated a “pass” result. For its welding joint, an applied stress of 55% YS generated a “fail” result while 50% YS generated a “pass” result, and the threshold stress will be between these two points.

The INDEX function in Microsoft Excel was used to generate an equation to fit the proof ring results. The INDEX function calculated the exponential curve that fitted the data from the proof ring experiments and returned an array of values that described the

curve. The generated equations were:

$$\% \text{YS to failure for the base steel} : \% \text{YS} = 33 \exp\left(-\frac{t}{35}\right) + 65 \quad (6)$$

%YS to failure for the welding joint

$$: \% \text{YS} = 43 \exp\left(-\frac{t}{11}\right) + 53 \quad (7)$$

Eq. (6) predicts that the threshold stress value of WDL690D base steel in the NACE TM-0177 “A” solution is 65% YS (or 364 MPa), and that of its welding joint in the above solution is 53% YS (or 296.8 MPa) as shown in Eq. (7). The base steel loaded

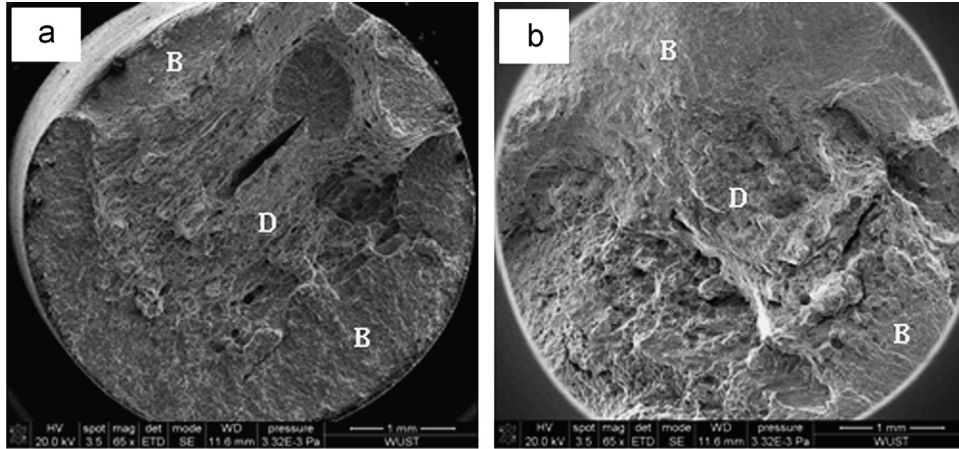


Fig. 9. Low magnification view of the specimen fracture surface: (a) the base steel applied stress of 72% YS and (b) the welded joint applied stress of 72% YS.

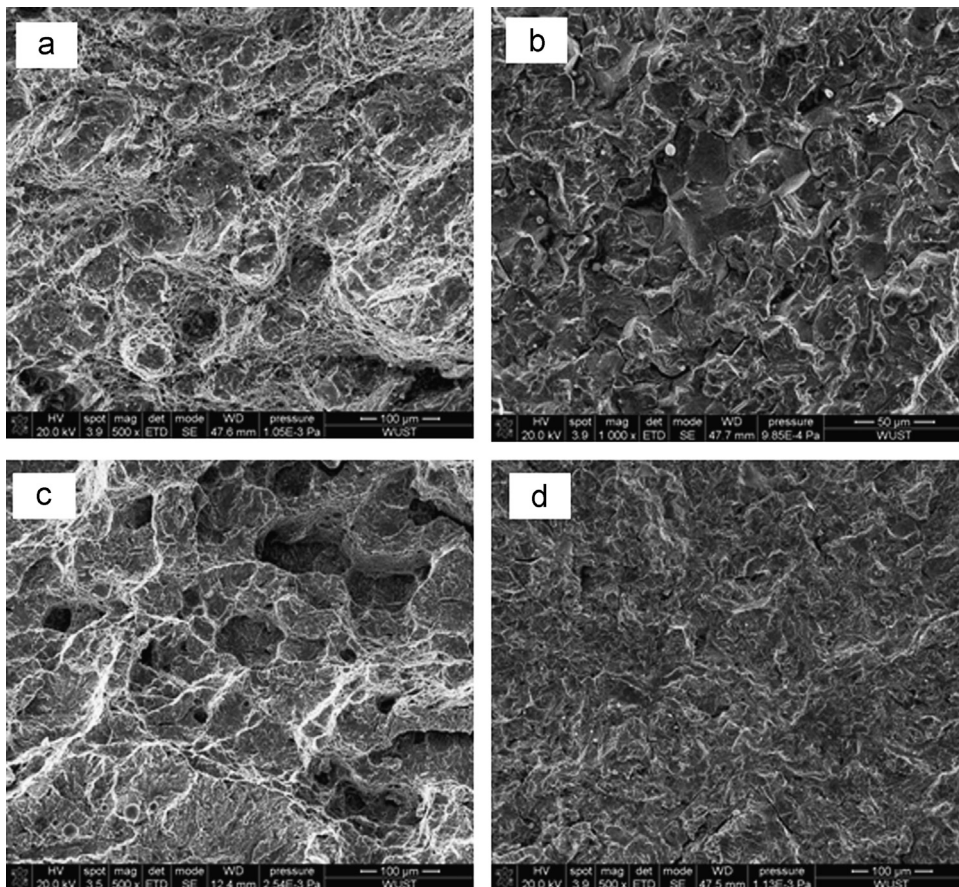


Fig. 10. The microcosmic fracture morphology of the specimen: (a) and (b) the base steel applied stress of 72% YS; (c) and (d) the welded joint applied stress of 72% YS.

below 65% YS, and the welded joint loaded below 53% YS should “always” pass the NACE TM-0177 test.

3.3.2. FE-SEM fractography analysis

Fracture surfaces were studied using FE-SEM after tensile test. Fig. 9(a–b) shows low magnification views of the WDL690D base steel and its welded joint failed tensile specimens in NACE TM-0177 “A” solution saturated with H₂S. Those two kinds of specimens exhibited nearly the same fracture, typical fraction of brittle regions connected by a ductile fracture region with secondary cracks on the fracture surface. Detailed observations of the fracture surfaces indicated that the ration of brittle to ductile areas of the welded joint specimen was light larger than that of the WDL690D base steel specimen.

Fig. 10 showed the microcosmic morphology of the fracture surfaces of the DWL690 base steel and its welded joint subjected to wet H₂S environment. It can be seen that the fracture surface of the base steel sample comprised of 100% ductile fracture morphology with dimples (Fig. 10a) and intergranular initiation region (Fig. 10b). However, for the welded joint sample, the fracture surface comprised of many micro-voids with a wide range of sizes, including large and deep dimples (Fig. 10c). Some brittle-like features could also be identified on the fracture surfaces, with the quasi-cleavage pattern being dominant (Fig. 10d). These features basically indicate the occurrence of brittle modes of fracture at local regions, most likely due to the presence of hydrogen and the inclusions in the two kinds of samples.

In addition, the non-metallic inclusions, acting as trapping sites to capture hydrogen, are the nucleation cores of the cracks, as seen in (Fig. 10b and d). Due to the synergistic effect of hydrogen and the non-metallic inclusions on the steel, cracks and quasi-cleavage fracture appeared around the inclusions (Fig. 10b and d) which indicated that cracks tended to initiate around the inclusions in a wet H₂S environment.

3.4. Hydrogen diffusion in WDL690D base steel and its welded joint

It has claimed that SSC and HIC susceptibility of steels have great relationship with hydrogen diffusion and trapping in the steels. The hydrogen permeation test can provide useful information on the hydrogen diffusion and trapping through the steel. The values of D_{app} , $J_{\infty}L$, c_{app} , and the hydrogen trap density N_T are measured and calculated from the hydrogen permeation transient curve. The

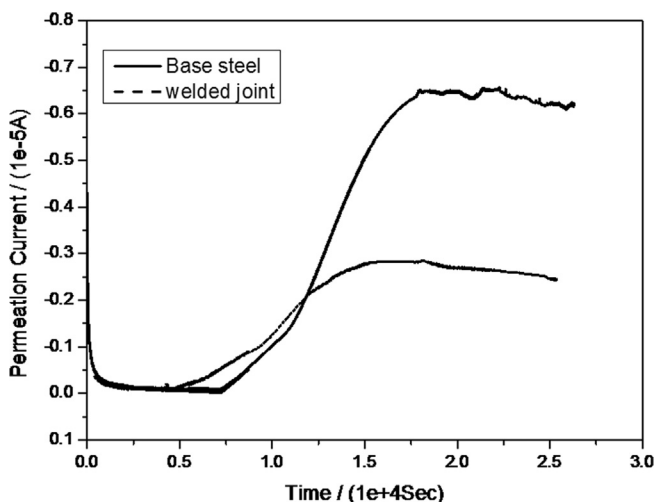


Fig. 11. Hydrogen permeation transient curves of WDL690 base steel and its welded joint.

Table 4

Hydrogen permeation data of different microstructure X80 steel.

Parameters	Sample	
	DWL690 base steel	The welded joint
I_{∞} (A)	4.88×10^{-6}	4.16×10^{-6}
t_L (s)	8031	9664
$J_{\infty}L$ (mol cm ⁻¹ s ⁻¹)	5.41×10^{-12}	4.61×10^{-12}
D_{app} (cm ² s ⁻¹)	2.37×10^{-7}	1.97×10^{-7}
c_{app} (mol cm ⁻³)	2.28×10^{-5}	2.33×10^{-5}
N_T (cm ⁻³)	2.46×10^{21}	3.03×10^{21}

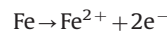
decrease in D_{app} , $J_{\infty}L$ and the increase in c_{app} , N_T suggest that more hydrogen can be entrapped in steel [22,26].

The hydrogen permeation curves of the WDL690D base steel and its welded joint specimen were determined in the NACE TM-0177 “A” solution saturated with H₂S as shown in Fig. 11. The calculated diffusion values of D_{app} , $J_{\infty}L$, c_{app} and N_T were listed in Table 4, which showed that the welded joint had smaller D_{app} , $J_{\infty}L$ values and larger c_{app} , N_T values than that of the WDL690D base steel, the implication was that the lower the values of D_{app} , $J_{\infty}L$ and the larger the value of c_{app} , N_T , the more the hydrogen trapping in the welded joint and the more the welded joint susceptible to SSC.

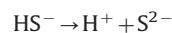
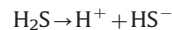
4. Discussions

In general, both the HIC and SCC of the pipeline steels in H₂S environments are closely related to the hydrogen trapping. The widely accepted corrosion reactions of steel exposed to a wet H₂S environment are [28]:

Anodic reaction:



Dissociation reactions:



Cathodic reaction:



Due to the poisoning effects of H₂S, hydrogen diffuses into the steel and does not proceed to undergo the recombination reaction on the steel surface. However, atomic hydrogen in the steel could accumulate in reversible (natural interstitial lattice sites) or irreversible traps (dislocations, grain boundaries, etc.) and recombine to form molecular hydrogen. When hydrogen pressure is up to a critical value, a crack will be initiated [29].

4.1. Effects of microstructure and hardness on SSC of WDL690D steel welded joint

Generally, it has been claimed that both hardness and microstructure influence the susceptibility of low alloy steels to hydrogen embrittlement through extensive work on the heat affected zones of welded steels [14]. Cracking initiates and propagates more easily in the less ductile microstructures. The results in this paper showed that the weld metal had highest hardness compared with other parts of the weld zone across the welded joint, as shown in Fig. 5. Therefore, at the same percentages of yield stress value of DWL690 based steel and its welded joint, the corresponding time-to-failure of the welded joint is much shorter than that of the base steel, as shown in Tables 3 and 4.

Previous researches of high strength low alloy steel confirmed that the SSC resistance in sort ascending was non-microalloyed acicular ferrite, non-microalloyed ferrite-pearlite, microalloyed ferrite-pearlite, microalloyed acicular ferrite and aged microalloy acicular ferrite [21], and bainite and martensite/austenite constituents deteriorated the workability of the welded specimens in sour environment [18]. The FE-SEM images in Fig. 4(a–d) suggest that the WDL690 base steel was typically ferrite and pearlite, with apparent austenite grain boundary network, but the microstructure of heat-affected zone and welded metal zone is very inhomogeneous, with the mixture of acicular ferrite, grain boundary ferrite, bainitic ferrite and a few M/A microconstituents. Surface local microscopical inhomogeneities of the welded joint could easily be hydrogen trapping sites and therefore were the predominant initiation sites of microcracks, resulting in the higher SSC susceptibility and shorter time-to-failure.

4.2. Effect of hydrogen and applied stress on the threshold stress of SSC

The SSC could be attributed to the injection of hydrogen into the specimen as forms as a by-product of the above corrosion reaction, directly related to a critical hydrogen concentration (C_H). The amount of hydrogen transported into the specimen is strongly influenced by the applied stress. According to Hirth [30], hydrogen penetration can be directly related to the applied stress in the specimens, because the highly localized stress could have induced hydrogen enrichment, which could be described by

$$C_H = C_0 \exp\left(\frac{\sigma_H V_H}{RT}\right) \quad (8)$$

where R is the gas constant, T is the absolute temperature, σ_H is the hydrostatic stress, and V_H is the partial molar volume of hydrogen. At the localized site of the applied stress, C_H can be enhanced significantly in comparison with the average value (C_0). When C_H reaches the critical value, the SSC occurs. As shown in Figs. 7 and 8, the failure time of the WDL690D base steel and its welded joint decreased with the increase of the applied stress, evidently indicating that higher the applied stress, more easily the SSC occurs.

In addition, when the applied constant stress is less than the intergranular cohesive strength, decreased by enriched hydrogen, no HIC occurs. Therefore, there exists a threshold stress below which no HIC occurs for constant charging conditions. As we all know, higher hydrogen concentration will lower cohesive strength at grain boundaries, so the threshold stress of HIC decreases with hydrogen concentration. As shown in Figs. 5 and 11 and in Table 4, for the welded joint specimen, the larger natural corrosion current, N_T and c_{app} value compared with WDL690D base steel specimen caused its higher SSC susceptible and lower threshold stress.

4.3. Effect of hydrogen on fracture characteristics

The present work showed that the fracture surface of the WDL690D base steel and its welded joint exhibited dimple mixed with quasi-cleavage fractures (Fig. 10). This type of fracture surface generally implied local areas of ductile fracture as well as areas of hydrogen-assisted crack propagation. When hydrogen was accumulated in a local area (Fig. 10b and d), hydrogen-assisted crack propagation was dominant, resulting in quasi-cleavage fractures. Otherwise, the cracks propagate by microvoid coalescence along the preferred crystallographic glide planes to form a ductile fractured morphology with dimples (Fig. 10a and c). Thus, the

areas of quasi-cleavage fracture increased with increasing diffusible hydrogen concentration, and the ratio of quasi-cleavage to ductile areas increased on the fracture surfaces of the welded joint which had a larger diffusible hydrogen concentration compared with the WDL690D base steel (as shown in Fig. 9a and b). As analyzed previously, the hydrogen concentration around inclusions was high, and quasi-cleavage fracturing would be likely to appear in the vicinity of inclusions (Fig. 10b and d).

5. Conclusions

- (1) For either WDL690D base steel or its welded joint, the failure time increased with the decreasing applied stress. The inhomogeneous microstructure distribution should be responsible for the lower threshold stress for the welded joint compared with WDL690D base steel.
- (2) The ability of the WDL690D base steel and welded joint to trap hydrogen was explained in terms of the apparent diffusivity (D_{app}), permeability ($J_{\infty}L$), and solubility of hydrogen in steel (c_{app}). The lower the values of D_{app} and the larger the value of c_{app} and N_T , the more the hydrogen was entrapped in the welded joint and the larger the SSC susceptibility of it.
- (3) The fractography of WDL690D base steel and its welded joint exhibited a mixed ductile-brittle rupture when exposed in H_2S environment under constant loading stress, and the area of quasi-cleavage fracture increased with increasing hydrogen concentration.

Acknowledgments

This work was supported by National Natural Science Foundation of China (No: 51201119) and Scientific Research Foundation of Hubei provincial education department (No: Q201211012).

References

- [1] Sarvesh Pal, R.K. Singh Raman, *Corr. Sci.* 51 (2009) 2443.
- [2] G.T. Park, S.U. Koh, H.G. Jung, *Corr. Sci.* 50 (2008) 1865.
- [3] A. Eslami, R. Kania, B. Worthingham, *Corr. Sci.* 53 (2011) 2318.
- [4] S.Q. Zheng, Y.M. Qi, C.F. Chen, *Corr. Sci.* 53 (2012) 59.
- [5] M. Al-Mansour, A.M. Alfantazi, M. El-boujdaini, *Mater. Des.* 30 (2009) 4088.
- [6] W.Y. Chu, *Hydrogen Damage and Delayed Cracking*, Metallurgical Industry Publishers, Beijing, 1988.
- [7] A. Kawashing, K. Hashimoto, S. Shimodaira, *Corr.* 32 (1976) 321.
- [8] J.L. Gonzalez, R. Ramirez, J.M. Hallen, *Corr.* 53 (1997) 935.
- [9] A.R. Troani, *Trans. ASM*, 52, 54.
- [10] R.A. Oriani, *Corr.* 43 (1987) 390.
- [11] H.Y. Liou, R.L. Shieh, F.L. Wei, *Corr.* 49 (1993) 389.
- [12] F. Huang, X.G. Li, J. Liu, Y.M. Qu, C.W. Du, *Mater. Sci.* 46 (2011) 715.
- [13] G. Domizzi, G. Anteri, J. Ovejero-García, *Corr. Sci.* 43 (2001) 325.
- [14] B. Beidokhti, A.H. Koukabi, A. Dolati, *Mater. Charact.* 60 (2009) 225.
- [15] F. Huang, X.G. Li, J. Liu, Y.M. Mao, *Mater. Cor.* 63 (2012) 59.
- [16] T. Hara, H. Asahi, H. Ogawa, *Corr.* 60 (2004) 1113.
- [17] M. Elboujdaini, V.S. Sastri, J.R. Perumareddi, *Corr.* 62 (2006) 29.
- [18] B. Beidokhti, A. Dolati, A.H. Koukabi, *Mater. Sci. Eng. A507* (2009) 167.
- [19] R.A. Carneiro, R.C. Ratnapuli, V.F.C. Lins, *Mater. Sci. Eng. A357* (2003) 104.
- [20] M.C. Zhao, Y.Y. Shan, F.R. Xiao, *Mater. Lett.* 57 (2002) 141.
- [21] M.C. Zhao, M. Liu, A. Atrens, *Mater. Sci. Eng. A478* (2008) 43.
- [22] G.T. Park, S.U. Koh, H.G. Jung, *Corr. Sci.* 50(2008)1865.
- [23] C.W. Du, X.G. Li, P. Liang, Y.F. Cheng, *Mater. Eng. Perform.* 18 (2009) 216.
- [24] Z.Y. Liu, X.G. Li, C.W. Du, G.L. Zhai, Y.F. Cheng, *Corr. Sci.* 50 (2008) 2251.
- [25] C.F. Dong, X.G. Li, Z.Y. Liu, Y.R. Zhang, *J. Alloys Compd.* 484 (2009) 966.
- [26] K.K. Banerjee, U.K. Chatterjee, *Scr. Mater.* 44 (2001) 213.
- [27] S.K. Yen, I.B. Huang, *Mater. Chem. Phys.* 80 (2003) 662.
- [28] M.A. Lucio-Garcia, J.G. Gonzalez-Rodriguez, M. Casales, *Corr. Sci.* 51 (2009) 2380.
- [29] T. Hara, H. Asahi, H. Ogawa, *Corr. Sci.* 60 (2004) 1113.
- [30] J.P. Hirth, *Metall. Mater. Trans. A11* (1980) 861.